




Investigation of structural and electrical properties of ITO thin films and correlation to optical parameters extracted using novel method based on PSO algorithm

RACHID AMRANI^{1,2,*} , ELYES GAROUDJA³, FOUAZ LEKOU^{2,4}, WALID FILALI³,
HAMID NEGGAZ¹, YACINE ADLANE DJEBELI¹, LAID HENNI⁴, SALIM HASSANI⁴,
FAOUZI KEZZOULA⁵, SLIMANE OUSSALAH⁶, FAISAL AL MASHARY⁷
and MOHAMED HENINI⁸

¹Département des sciences de la matière, Université Alger1 Benyoucef Benkhedda, Alger, Algeria

²LPCMME, Département de physique, Université d'Oran 1, Oran, Algeria

³Plateforme Technologique de Micro-fabrication, Centre de Développement des Technologies Avancées, Cité 20
Août 1956, Baba Hassen, Alger, Algeria

⁴Division milieux ionisés and Laser, Centre de Développement des Technologies Avancées, Cité 20 Août 1956,
Baba Hassen, Alger, Algeria

⁵CRTSE -Division DDCS, 2 Bd Dr Frantz Fanon BP 140 Alger – les sept merveilles, Alger, Algeria

⁶Division Microélectronique and Nanotechnologies, Centre de Développement des Technologies Avancées, Cité 20
Août 1956, Baba Hassen, Alger, Algeria

⁷Department of Physics, College of Science, Qassim University, 14452 Buraydah, Saudi Arabia

⁸School of Physics and Astronomy, University of Nottingham, Nottingham NG7 2RD, UK

*Author for correspondence (rachidamrani2002@yahoo.fr; r.amrani@univ-alger.dz)

MS received 18 May 2022; accepted 29 August 2022

Abstract. Thermally annealed DC sputtered indium tin oxide (ITO) thin films were investigated for improvement in properties. The structural and optoelectronic characteristics of as-grown and air annealed films were studied and correlated to the film deposition time. Raman spectroscopy analysis showed low crystalline quality films for as-grown films and were significantly improved after annealing. X-ray diffraction analysis confirmed the crystallinity of samples with (222) preferential orientation. The 30-min ITO films showed a peak at (400). The films optical study shows an increased transmittance (in the transparency region) with decreasing deposition time, yielding a high transparency of 90% for the 5- and 15-min ITO films annealed at 400°C. The films thickness and optical constants were determined from optical transmission only without interference fringe using a novel method based on particle swarm optimization (PSO) algorithm. The absorption coefficient and calculated refractive index decreased with increasing deposition time and their value reduced further after annealing treatment. The 30-min ITO films showed a comparable low resistivity of $4 \times 10^{-3} \Omega \text{ cm}$ before and after annealing as determined by Hall effect measurements. This observation confirms their non-sensitivity to the oxygen post-contamination that resulted from (400) orientation. A shift of the absorption edge towards shorter wavelengths accompanied with an increase in the optical bandgap before and after annealing with decreasing thickness were observed. We have demonstrated that the optical parameters such as the optical gap depend mainly on the electrical parameters such as the carrier concentration.

Keywords. ITO thin films; DC sputtering; deposition time; Raman spectroscopy; optical and electrical properties; PSO algorithm.

1. Introduction

Sn-doped In_2O_3 , which is known as indium tin oxide (ITO), has become an important material for various applications due to its specific properties such as the unification of high electrical conductivity and high transparency [1–3]. It is one of the most studied transparent conductive oxide (TCO) due to its low resistivity as compared to other TCOs, such as

ZnO and SnO_2 [4,5]. Its behaviour as a TCO is the result of its n-type semiconductor nature and a wide bandgap ranging from 3.5 to 4.3 eV [6]. ITO has a low resistivity, generally varying between 10^{-3} and $10^{-4} \Omega \text{ cm}$, which is caused by two essential factors, namely, (i) oxygen vacancies, which facilitate the electronic transport by introducing additional levels into the forbidden band [7], and (ii) Sn substitutional incorporates into the In_2O_3 lattice and creates a negative

carrier excess because Sn^{4+} ions create fewer bonds than In^{3+} ions, and hence, there will be more free charge carriers, resulting in a significant increase in the Fermi level [8].

Many works have studied ITO thin films using different deposition techniques [9–13]. Pankratz [14] was one of the first to work on the ITO in 1972. To optimize the optical and electrical properties of the ITO thin films, he deposited samples with different Sn mass percentages by RF sputtering using an argon–oxygen gas mixture during deposition with different proportions followed by annealing at 500°C. His study proved that the argon–oxygen gas ratio has much more influence than the In/Sn mass ratio on the properties of the RF sputtered ITO layers. Also found that the optimal ratio of argon: oxygen gas is 82:18. Pankratz [14] obtained ITO films with a transparency of 95% and a resistance square which can reach $300 \Omega \text{ Sq}^{-1}$ before annealing and $200 \Omega \text{ Sq}^{-1}$ after annealing. Mizuhashi [15] studied the electrical properties of the ITO deposited by evaporation as a function of the mass percentage of Sn and the substrate temperature. He obtained by evaporation of an ITO thin film with a resistivity of $2.10\text{--}4 \Omega \cdot \text{cm}$ and a Hall mobility $\mu_{\text{H}} = 72 \text{ cm}^2 \text{ V}^{-1} \text{ s}^{-1}$ for the 5% Sn layer annealed at 400°C. In order to optimize optical transparency, Minami *et al* [16] are interested in studying the different effects of annealing and concentrations on the ITO thin films. To do this, they deposited thin layers of the same thickness using the DC magnetron sputtering with different targets containing different SnO_2 doping (0, 1, 5 and 10%). The results before annealing showed that the increase in doping considerably reduced the transparency. They demonstrated that annealing was able to solve this transparency problem where they obtained a transparency of more than 90%. Torkaman *et al* [17] are interested in the influence of annealing at 450 and 500°C under vacuum for 1 h on the properties of ITO layers. They demonstrated that the layers have a nanocrystalline structure and the increase in annealing temperature led to an increase in the crystallites size as well as the conductivity and the concentration of carriers. Chen *et al* [18] have studied the influence of the oxygen flux used in the deposition of thin layers of ITO by DC magnetron sputtering with various oxygen flow rates. They showed that the oxygen concentration detected by XPS in the ITO films increases with the oxygen flow. By calculations, using the density functional theory, they demonstrated that the increase in oxygen vacancies induces the increase in the bands below the Fermi level as well as the presence of a second bandgap.

Among all these works, the DC or RF magnetron sputtering method is most often used to produce ITO thin layers. ITO layers deposited by the DC/RF magnetron sputtering method generally require a low partial pressure of oxygen when alloy and oxidized targets are used. In this work, the ITO thin films deposited by DC sputtering of InO_2 -Sn target using Argon plasma without oxygen in the sputtering process. To evaluate the effects of deposition time and thermal annealing on the structural and optoelectronic properties of

ITO thin films, the deposition time was varied for 5, 10, 30 and 60 min. One series of the resulted films was further air annealed at 400°C for 1 h. X-ray diffraction (XRD) and Raman spectroscopy were used to characterize the structural properties of the ITO films. The optical properties of the thin films were analysed from optical transmission measurement. In all transmission spectra of ITO thin films studied in this work, no interferences fringes are observed. The determination of the optical constants from the classical envelope method cannot therefore be carried out. In this article, we developed novel method based on the particle swarm optimization (PSO) algorithm [19,20] for the extraction of thickness and the optical constants, such as the dispersion of the refractive and the optical absorption coefficient from optical transmission spectra only. The optical bandgaps were determined from optical absorption coefficient spectra using the Tauc extrapolation method. Finally, the electrical characteristics, namely resistivity, carrier concentration and mobility, were determined using the Hall effect technique. The correlation between the films' optical bandgap and the electrical characteristics, and particularly the effective mass, carrier concentration and mobility, has been well investigated.

2. Experimental

ITO films were grown on glass substrates of a 1 mm thickness and a $25 \times 75 \text{ mm}^2$ surface area with a homemade physical vapor deposition (PVD) DC sputtering system using only argon in the sputtering process. The electrode diameter and the distance between the electrodes were 45 and 40 mm, respectively. The used ITO target (90% InO_2 and 10% Sn) with a 60 mm diameter and 2.5 mm of thickness had a purity of 99.99%. The substrates were first cleaned with acetone and ethanol for 5 min and then introduced into the sputtering chamber. This was followed by introducing argon (Ar) as an inert gas until the chamber reached a minimum background pressure of 1.7×10^{-5} Torr. The sputtering conditions were adjusted to 5×10^{-1} Torr as the working pressure and 40 W of input power for all experiments. For all the deposited layers, the substrates were kept at room temperature while the deposition time was set to 5, 15, 30 and 60 min to obtain four different thicknesses. Once the deposition process is done, two series of samples have been prepared. The first one consists of samples 5, 15, 30 and 60 as-grown, while the other series consists of exactly the same samples but all have been air annealed at 400°C for 1 h at a heating rate of $10^\circ\text{C min}^{-1}$. The structural, optical and electrical properties before and after annealing treatment were then investigated. The structural properties of the deposited ITO films were investigated by means of XRD technique in standard Bragg-Brentano configuration (θ - 2θ) at room temperature using Philips X'Pert MPD diffractometer with conventional $\text{Cu-K}\alpha$ X-ray radiation ($\lambda_{\text{XRD}} = 1.54056 \text{ \AA}$). The bonding

structure and crystallinity was also characterized by Raman scattering measurement. Raman spectra were measured in backscattering geometry with Horib Jobin-Yvaon confocal LabRam H-Resolution micro-Raman with a laser at wavelength of 325 nm. The power of laser was kept below 200 μW to avoid laser-induced crystallization on the films. The peak positions were determined with accuracy below 0.3 cm^{-1} after curve fitting. The electrical characteristics, namely the resistivity, carrier concentration and mobility were determined from Hall effect measurements using a HL5900PC Hall effect profiler. The optical transmittance of the deposited layers was measured by OPTIZEN 3220 UV spectrophotometer in UV-visible-NIR range (200–1100 nm). The film thickness and optical constants of the samples were extracted from the measured optical transmission spectra by using an efficient PSO algorithm-based method.

3. Results and discussion

3.1 Structural properties

Figure 1 shows Raman spectra of the ITO layers grown with different deposition times before and after annealing. Four characteristic peaks of In_2O_3 at 112, 135, 172 and 319 cm^{-1} [6] are clearly seen. A fifth peak was identified at 575 cm^{-1} , which corresponds to SnO_2 vibration modes [21].

A comparison of the full-width at half-maximum (FWHM) of the Raman peak at 319 cm^{-1} shows much higher values than those reported previously, indicating that the films have higher stress and lower crystallinity. However, after annealing, these values decrease, indicating an improvement in the layer crystallinity. The existence of 575 cm^{-1} peak was reported by Diéguez Barrientos *et al* [21] in nanometric SnO_2 . The comparison of the peak evolution before and after annealing clearly shows its disappearance in deposited samples with 30 and 60 min after annealing. This could be explained by the fact that the ITO film crystallization goes through a stage where Sn atoms must find a position where they are in stable thermodynamic equilibrium by replacing indium [22].

Figure 2 shows the XRD spectra of all samples after annealing. These results show that the samples deposited above 15 min exhibit crystallinity. The spectrum of the layer deposited for 5 min shows no peak. This is probably due to the low thickness value. The identification of (211), (222), (400), (411), (332), (431), (440) and (622) directions can be indexed as the characteristic structure of the cubic ITO phase according to (JCPDS File No. 6 416) [23]. Thermalized atoms promote crystallization in orientation (222), but excess energy causes crystallization along the (400) and (440) planes [24]. We note that our layers have a preferential orientation (222). This orientation is demonstrated by comparing the I222/I400 intensity ratio of the

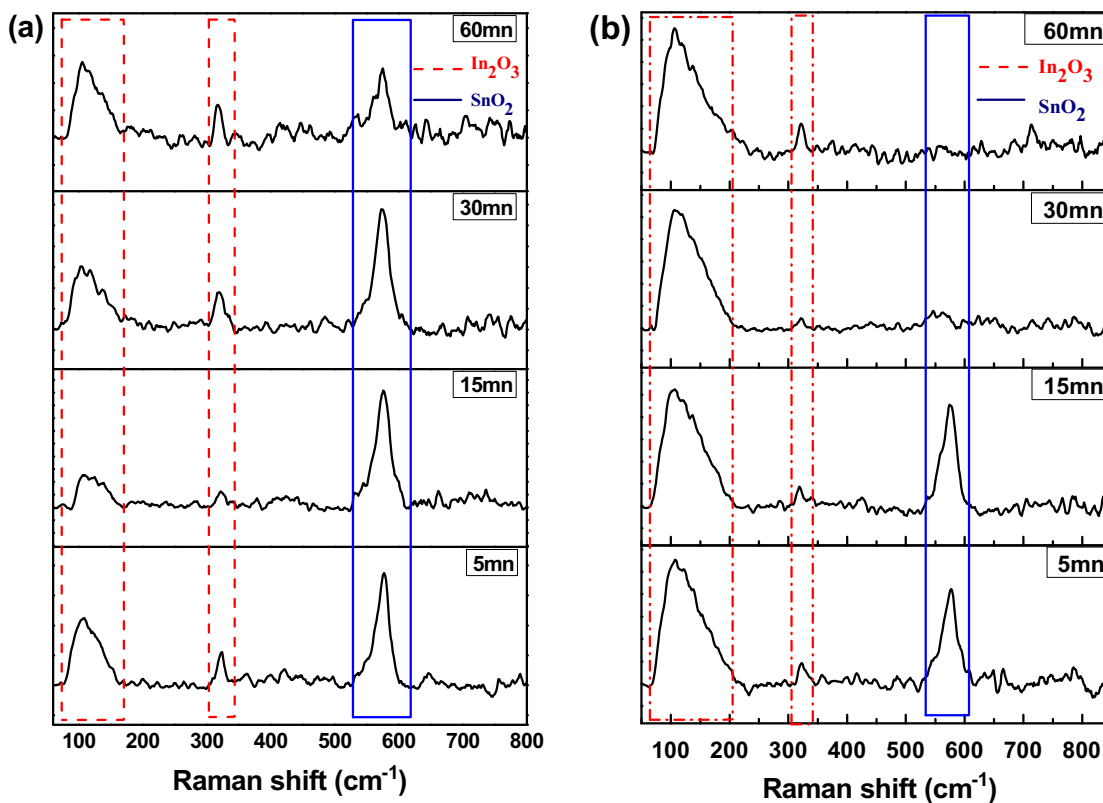


Figure 1. Raman spectra of ITO layers (a) before and (b) after annealing.

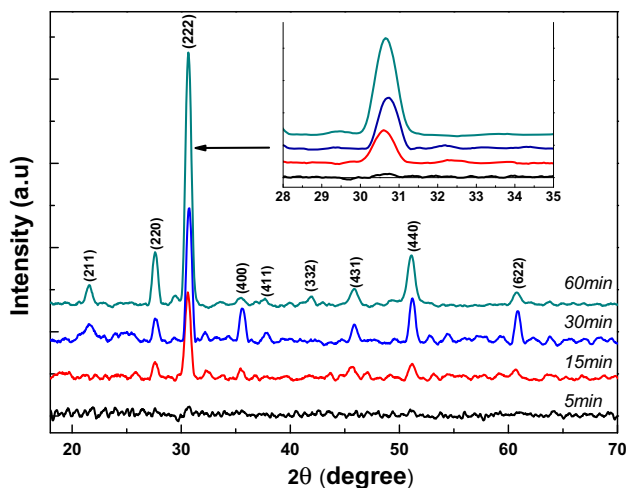


Figure 2. XRD spectra of all samples after annealing.

XRD spectra of our samples to that of samples by Le *et al* [25]. Table 2 shows the values of this ratio. For all samples, this ratio is higher than the reference value of 3.33. This preferential orientation is more pronounced in the sample deposited for 60 min. Shakiba *et al* [26] have shown that the oxygen vacancies are more important and apparent in the plane (400) than in the plane (222).

It is noticed that the sample deposited for 30 min seems to have a different structure than the others. In fact, it has a high peak intensity corresponding to the (400) direction. The value of the I_{222}/I_{400} ratio for the 30 min layer is smaller than the other layers, which could be due to a microstructure change as reported by Lee and Park [22], who studied the relationship between surface roughness and the I_{222}/I_{400} ratio. It was shown that the roughness decreased when the I_{222}/I_{400} ratio increased. According to Dong *et al* [27], this peak causes aggregation of grain growth along the (400) plane, resulting in higher surface roughness.

For further investigation into the structural modifications, the lattice parameter ‘ a ’ was calculated using the Bragg relation [28]:

$$n\lambda = 2d_{hkl} \sin(\theta_{hkl}) \quad (1)$$

where h , k and l are Miller indices, θ_{hkl} is the diffraction angle, d_{hkl} and n are the inter-planar distance and diffraction order ($n = 0, 1, 2, \dots$), respectively. In the cubic structure of ITO, the inter-planar distance d_{hkl} is given by [29]:

$$d_{hkl} = \frac{a}{\sqrt{h^2 + k^2 + l^2}} \quad (2)$$

when $n = 1$, at the first order of approximation, the values of ‘ a ’ are expressed by:

$$a = \frac{\sqrt{3}}{\sin \theta_{hkl}} \quad (3)$$

For further understanding of the structural changes, the microstrain τ was determined by using the equation [6]:

$$\tau = \frac{FWHM \cos \theta}{4} \quad (4)$$

where FWHM and θ are full-width at half-maximum of XRD spectra and Bragg diffraction angle, respectively. To determine these parameters, (222) peaks for ITO annealed films were selected. The results are summarized in table 1.

It is noted that the value of the lattice parameter of the 60-min layer is greater than 10.118 Å, which corresponds to that of pure In_2O_3 . This increase in the lattice constant of ITO film can be explained by the substitutional incorporation of Sn^{4+} ions into the sites of In^{3+} . This can lead to an expansion of the lattice and/or the incorporation of Sn ions in an interstitial position. Deformations in the lattice can be created because the radius of Sn^{4+} ions (~ 0.93 Å) is greater than that of In^{3+} (~ 0.79 Å) [30].

3.2 Optical properties

The optical transmission spectra in the wavelength range of 200–1100 nm of ITO layers before and after annealing are shown in figure 3a and b, respectively. As clearly seen, these spectra consist of three zones: (i) strong absorption between 200 and 290 nm, (ii) weak absorption between 290 and 400 nm, and (iii) zone of transparency from 400 to 1100 nm. The optical transmission values remain almost constant in the transparency region, and these values vary between 74 and 90%, depending on the deposition time. By comparing these spectra, it can be seen that the transparency is related to the deposition time and therefore to the thickness of the layers. The value of the transmission in the transparency zone decreases with the increase in the deposition time. On the other hand, the transmission spectrum of the deposited layer for 30 min shows a lower value of transmission than that obtained from the deposited layer for 60 min. The transmission spectrum of the deposited layer for 30 min (figure 3a) is an apparent transmission spectrum, not the true transmission. Indeed, it can be observed that the transmission of this layer is not constant in the transparency zone, a fact that indicates that it has a high surface roughness [31,32]. Figure 3b shows that after annealing, there is an increase in optical transmission for all samples, indicating an improvement in the transparency of the elaborated layers. The deposited layer for 30 min showed the most remarkable increase of 9% at $\lambda = 650$ nm and reached the same transparency as that of the sample deposited for 60 min. Moreover, the optical transmission of the deposited layer for 30 min after annealing is also not constant in the transparency region. This can be explained by the existence of a large surface roughness on this sample. This is in good agreement with XRD results in terms of the strong intensity of the (400) peak [22,27]. As previously mentioned, the annealing process improves the transparency of the layers,

Table 1. Results obtained from XRD analysis.

Time (min)	Ratio I_{222}/I_{400}	θ ($^\circ$)	FWHM (rad)	Mesh parameter 'a' (Å)	Microstrain (10^{-3}) GPa
15	9.5	15.3	0.01	10.1	2.5
30	4.16	15.36	0.01	10.06	2.55
60	35	15.33	0.01	10.89	2.65

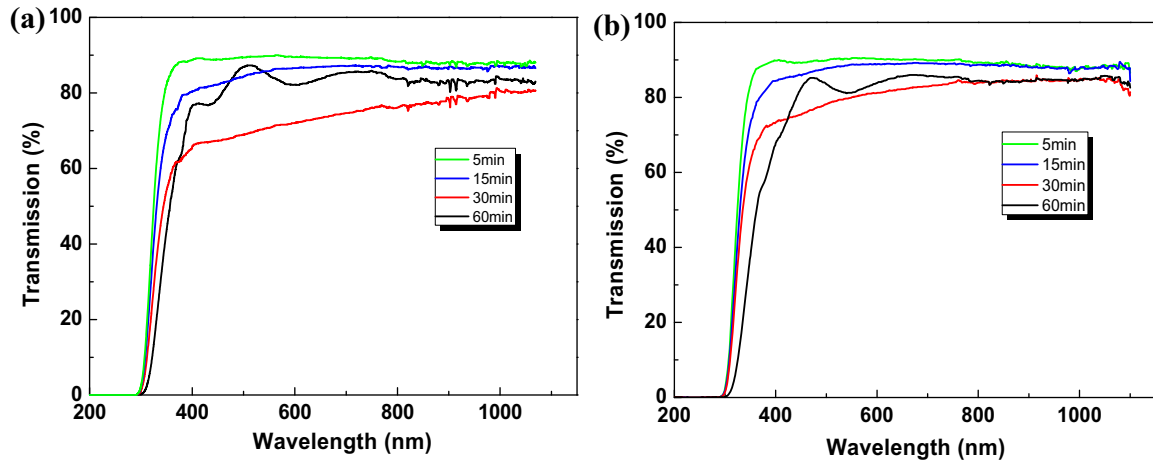


Figure 3. Optical transmission for ITO films (a) before annealing and (b) after annealing.

as reported previously [33]. However, the transmission spectrum of a 30-min sample after annealing has a lower variation in the transparency zone than before annealing. This can be explained by a decrease in surface roughness. The increase in transmission may be due to the decrease in diffuse reflection.

It is important to point out that interference fringes in all transmission spectra were not observed. Therefore, the determination of the thickness and dispersion of the refractive index as well as the optical absorption coefficient from the envelope methods proposed by Manificier *et al* [34] and Swanepoel [35] becomes impossible. In theory, reflection measurements must be performed in addition to transmission measurements to determine the optical constants [31,32]. In this work, we developed a method for the determination of optical constants from transmission measurements only based on an efficient heuristic calculation method [36]. Lekoui *et al* [20] investigated the optical properties of nanostructured Mn-doped ZnO thin films by applying an efficient optimization algorithm called particle swarm optimization (PSO) proposed by Eberhart and Kennedy [19,37]. The crucial idea of this method is to deal with the problem of determining the optical properties from an optimization point of view. In other words, the objective (cost) function to be minimized was first defined. Afterwards, the PSO algorithm begins to seek the optimal solution (minimizing the cost function) in an iterative way until reaching convergence. The objectives function to be optimized using the PSO algorithm is defined as the root mean

square error (RMSE) between the measured and estimated transmittance spectra. The estimated transmittance spectrum is computed from equations (5–11) [36,38] after having replaced the identified parameter values, while the cost function to be minimized is given by equation (14).

$$T = \frac{Ax}{B - Cx + Dx^2} \tag{5}$$

where

$$A = 16n_s(n^2 + k^2) \tag{6}$$

$$B = [(n + 1)^2 + k^2] [(n + 1)(n + n_s^2) + k^2] \tag{7}$$

$$C = [(n^2 - 1 + k^2)(n^2 - n_s^2 + k^2) - 2k^2(n_s^2 + 1)] 2 \cos \varphi - k[2(n^2 - n_s^2 + k^2) + (n_s^2 + 1)(n^2 - 1 + k^2)] 2 \sin \varphi \tag{8}$$

$$D = [(n - 1)^2 + k^2] [(n - 1)(n - n_s^2) + k^2] \tag{9}$$

$$\varphi = \frac{4\pi nd}{\lambda} \tag{10}$$

$$x = \exp(-\alpha d) \tag{11}$$

n_s denotes the substrate refractive index, n is the thin film refractive index, k and α are the thin film extinction and absorption coefficients, respectively. d denotes the thin film optical thickness. In order to compute the refractive index

of ITO films, Cauchy dispersion model has been employed and it is given as follow [36]:

$$n(\lambda) = \alpha_1 + \frac{\beta_1}{\lambda^2} \quad (12)$$

$$k(\lambda) = \alpha_2 + \frac{\beta_2}{\lambda^2} \quad (13)$$

where α_1 , α_2 , β_1 and β_2 are the model fitting parameters.

$$\text{RMSE} = \sqrt{\sum_{j=1}^m [T_{\text{Meas}}(j) - T_{\text{Est}}(j, \omega)]^2 / L} \quad (14)$$

T_{Meas} and T_{Est} in equation (14) denote, respectively, the measured and estimated transmittance data. ω is the vector of parameters to be determined and it includes Cauchy dispersion model coefficients and optical thickness ($\omega = [\alpha_1, \beta_1, \alpha_2, \beta_2, d]$). L represents the size of transmittance spectrum vector.

The PSO algorithm, which is a powerful heuristic search method, is based on the swarming behaviour of biological populations, such as birds and fishes. This choice is due to the fact that PSO is widely applied to solve many number of optimization problems in different areas [39,40]. The proposed strategy used in this work is summarized in figure 4.

To accurately determine the optical properties, the PSO algorithm will be initially employed for medium and weak absorption zone transmittance spectra, with the aim of obtaining the optical thickness and Cauchy model parameters. The refractive index values that correspond to the entire wavelength range will then be calculated using equation (12). The obtained thickness, d , using the PSO method of elaborated samples for 5, 15, 30 and 60 min was 3, 25, 71 and 173 nm, respectively. Annealing had no influence on the thickness of the samples.

Figure 5a shows the variation of the refractive index, n , of the elaborated samples before annealing as a function of wavelength λ . A decrease in the refractive index with increasing deposition time and therefore with thickness was observed. Figure 5b shows that for as grown samples, the static refractive index n_0 decreases with increasing

deposition time. After annealing, the values of n_0 decreased for all samples compared to the as-deposited samples. On the other hand, it can be seen that the layers after annealing have almost the same static refractive index (1.69–1.81).

Figure 6a shows the influence of the deposition time on the optical absorption coefficient as a function of photon energy. The absorption coefficient α was obtained from the strong absorption zone as follows [34,35,41]:

$$\alpha = -\frac{1}{d} \ln\left(\frac{B}{A} T\right) \quad (15)$$

It is noticeable that the absorption coefficient decreases with the increase of the deposition time. Figure 6b shows the influence of annealing on absorption for the deposited layer for 30 min. A remarkable decrease in absorption after annealing was observed. This result is in good agreement with the result obtained from the improvement of the layer's transparency with annealing.

According to Torkaman *et al* [17] and Song *et al* [42], crystalline ITO is a direct gap semiconductor. From the absorption coefficient, the optical gap E_g can be extracted using the extrapolation method proposed by Tauc [41]:

$$(\alpha h\nu)^2 = A(h\nu - E_g) \quad (16)$$

An example of extraction of the direct optical gap for the deposited layer with a time of 15 min is shown in inset of figure 7.

The results of the optical gap obtained for all samples, before and after annealing, are summarized in figure 7. Before annealing, the direct optical gap values are around 4 eV, which is in perfect agreement with the literature [42,43]. There is a slight decrease in the gap with increasing deposition time. On the other hand, the annealing process has no significant effect on the gap variation.

3.3 Electrical properties

The results of Hall electrical measurements are summarized in table 2. It is worth pointing out that 5-min sample is not shown in table 2 due to its very low thickness ~ 3

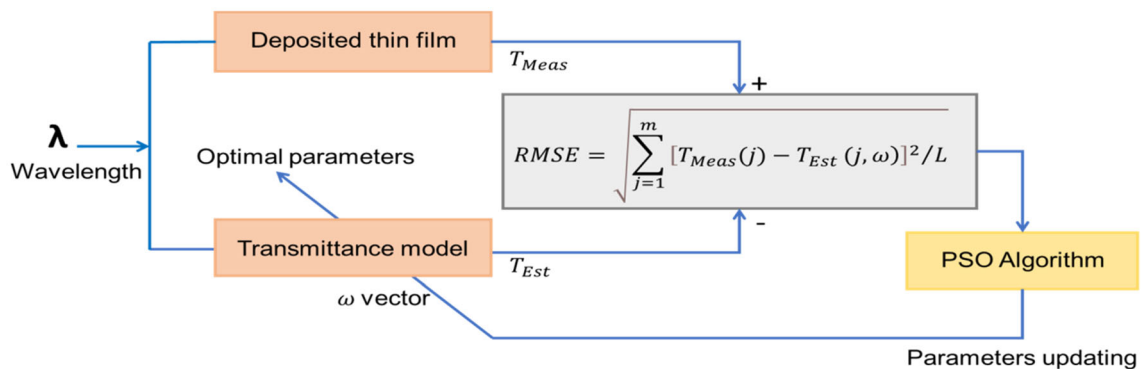


Figure 4. Method for determining the film thickness and optical constants.

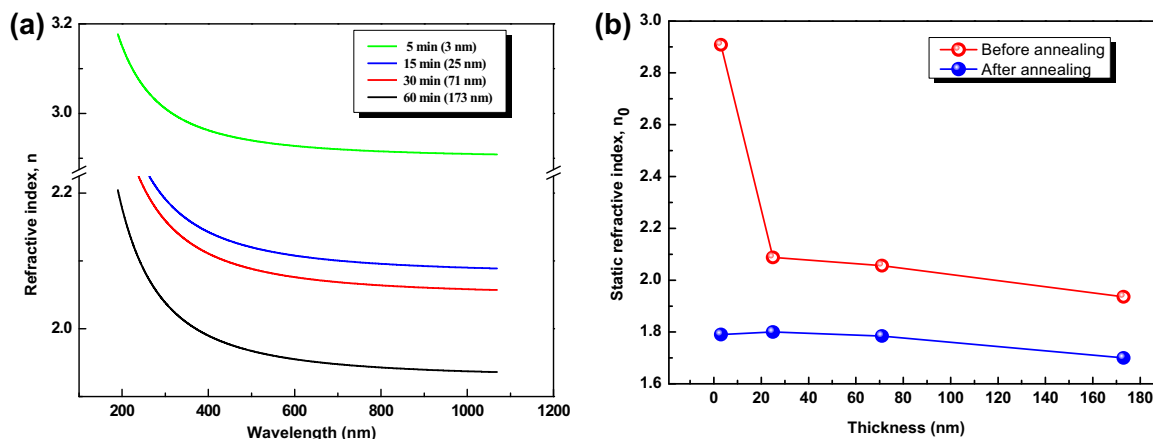


Figure 5. (a) Evolution of the refractive index as a function of wavelength for different ITO film thicknesses before annealing. (b) Variation of the static index n_0 as a function of ITO film thickness before and after annealing.

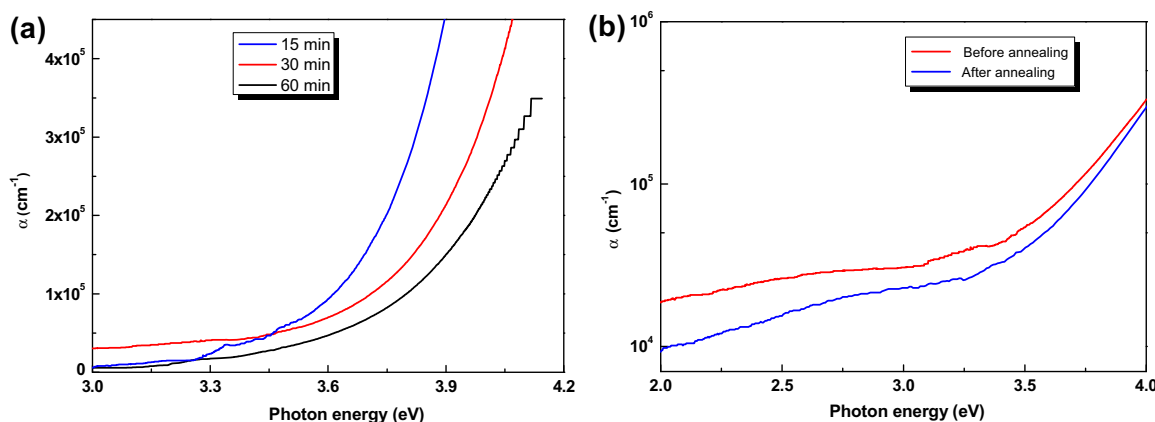


Figure 6. (a) Evolution of the optical absorption coefficient as a function of energy for different ITO film thicknesses. (b) Absorption coefficient evolution as function of energy before and after annealing of sample deposited for 30 min.

nm. Hall effect results have shown that all ITO layers are *n*-type. This result was also confirmed by the hot tip technique.

A significant increase in electron mobility of as-grown samples with deposition time is observed. This enhancement of the Hall mobility may be due to the diffusion of carriers at the grain boundaries as suggested by Lee and Park [22], where a space charge region was reported at the interface between the grains. The electronic transport takes place primarily through the amorphous matrix in the material, in the grain boundaries [44]. As clearly seen in table 2, the mobility of the annealed samples is in general lower than that of the as-grown samples except 15 min sample, which can be explained by an increase of the crystallite sizes after annealing, as confirmed by Raman measurements. This increase in crystallite sizes can lead to the deterioration of the amorphous phase quality in the grain boundaries, caused by the substitution of In atoms by Sn and the creation of vacancies. For a 15-min deposited layer, the variation in the mobility is not significant because of the small layer thickness.

The carrier density *vs.* ITO film thickness for as-grown and annealed samples is also shown in table 2. Before annealing, the carrier density decreases as the thickness of the samples increases. This reduction can therefore be related to the increase in mobility. After annealing, an apparent decrease was observed in carrier density values for 15- and 30-min deposition samples as compared to their values before annealing. On the contrary, for the 60-min deposited sample, a large increase of carrier density can be clearly seen in table 2. After annealing, oxygen vacancies and Sn⁴⁺ active states are created. Oxygen vacancies and Sn substitution will increase the possibility of free electron generation [22]. For thin layers of 20–80 nm in thickness, the density and size of vacancies are very small. The contribution of these vacancies to the generation of charge carriers after annealing becomes negligible. After crystallization of these layers, the contribution of the amorphous phase in the grain boundaries to the capture of charge carriers becomes more important. This could explain the decrease in carrier density after annealing of the two samples deposited with 15 and 30 min.

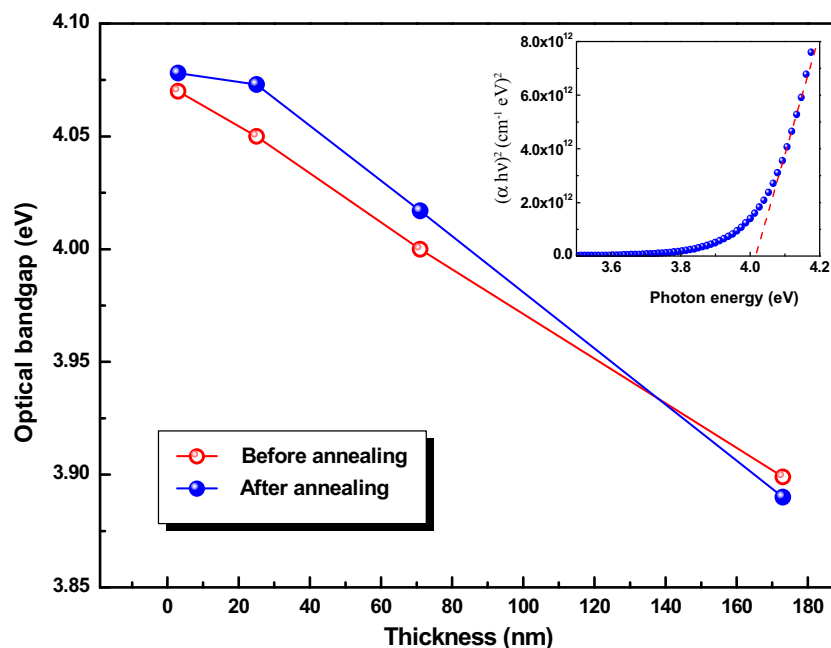


Figure 7. Optical bandgap obtained for all samples before and after annealing. Inset is an example of determination of the Tauc optical gap of the deposited sample for 15 min.

Table 2. Hall electrical measurement results.

Deposition time (min)	Optical thickness (nm)	Mobility ($\text{cm}^2 \text{V}^{-1} \text{s}^{-1}$)		Resistivity ($\text{m}\Omega \text{cm}$)		Carrier concentration 10^{20}cm^{-3}	
		Before annealing	After annealing	Before annealing	After annealing	Before annealing	After annealing
15	25	0.20	0.58	2.77	46	10.98	2.24
30	71	1.82	0.30	4.07	4.56	8.42	2.88
60	173	19	0.32	53.92	14	0.59	13.7

For the resistivity of layers before annealing (table 2), we notice a little increase from 2.7 to 4 $\text{m}\Omega \cdot \text{cm}$ when the thickness varies between 25 and 70 nm. However, for the 173-nm thick sample, there was a significant increase in its resistivity (53.9 $\text{m}\Omega \cdot \text{cm}$) as compared to the other two samples. Concerning the ITO layers after annealing, a decrease in resistivity of the deposited sample for 60 min may be due to the large decrease in mobility from 19 to 0.3 $\text{cm}^2 \text{V}^{-1} \text{s}^{-1}$ with a very large increase in charge density from 0.6×10^{20} to $13.7 \times 10^{20} \text{cm}^{-3}$. The increase in resistivity for the sample of 15-min deposition time is due to the large decrease in the charge density from 11×10^{20} to $2.2 \times 10^{20} \text{cm}^{-3}$ accompanied by a slight increase in mobility from 0.20 to 0.58 $\text{cm}^2 \text{V}^{-1} \text{s}^{-1}$. On the other hand, regarding the deposited layer for 30 min, both mobility and charge density follow the same behaviour. Their values decrease from 1.8 to 0.3 $\text{cm}^2 \text{V}^{-1} \text{s}^{-1}$ and from 8.4×10^{20}

to $2.8 \times 10^{20} \text{cm}^{-3}$, respectively. This may explain the small variation in resistivity for this sample. This can be caused by its preferential direction along the crystal axis (400) as demonstrated by XRD analysis. Under this circumstance, this deposited layer is insensitive to oxygen contamination as opposed to other layers, which have a preferential orientation (222). Therefore, the crystalline direction (400) is less sensitive to the oxygen contamination than (222) direction [26].

It can be noticed that by increasing the ITO layer thicknesses, a shift in the absorption edge towards greater energy values in the near-ultraviolet and visible wavelength regions was observed in transmission spectra. It is known as the Burstein-Moss effect [43] and it can be given by equation (17). This is due to the change in the optical gap, which is mainly caused by the variation of carrier concentration.

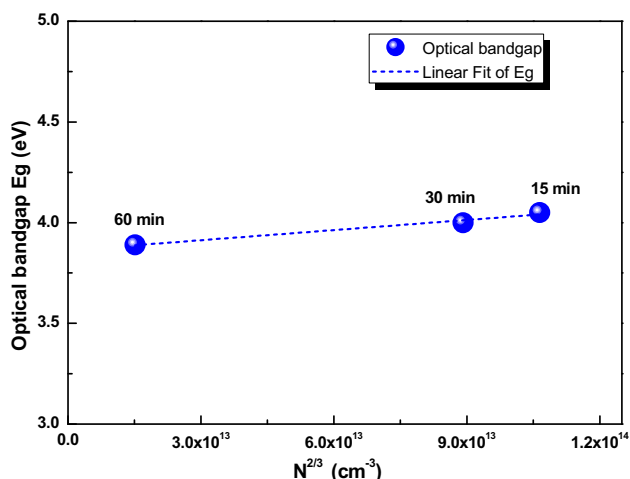


Figure 8. Optical bandgap as functions of charged carrier concentration for ITO films before annealing.

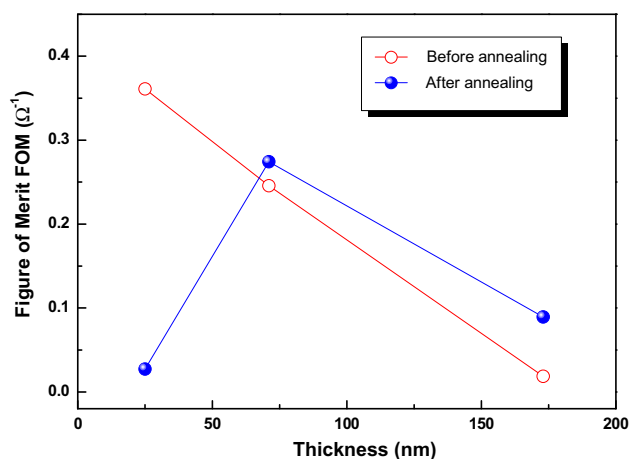


Figure 9. Variation of the figure of merit factor as a function of ITO film thickness before and after annealing.

$$E_g - E_{g0} = \frac{(\pi h)^2}{2m_r^*} \left(\frac{3N}{\pi} \right)^{2/3} \quad (17)$$

where E_g is the samples optical bandgap, E_{g0} is the intrinsic optical gap, N denotes the carrier concentration and m^* is the reduced effective mass. Figure 8 shows the variation of optical gap as function of carrier concentration before annealing.

There is a linear dependence between the optical gap and carrier concentration. The value of E_{g0} was estimated as 3.86 eV by extrapolating the charge density value to zero from the linear fit. The obtained values of intrinsic optical gap of ITO films are in good agreement with those found by previously published works [45–48]. From the linear fit in figure 8, a low value of effective mass ($m^* = 0.86 m_0$) was obtained for the samples before annealing. This result is in agreement with the results obtained by Ray *et al* [47] and Ohhata *et al* [48]. After annealing, there is an increase in the intrinsic optical gap ($E_{g0} = 4.12$ eV) and a decrease in the

effective mass ($m^* = 0.76 m_0$). This is due to the layers' crystallization and the possibility of oxygen incorporation in grain boundaries for samples during air annealing.

The selectivity of a TCO film comes from a compromise between these transparency and conductivity properties. In order to predict the TCO selective properties from the fundamental optical and electrical properties, the figure of merit can be employed. Haacke [49] already proposed in 1976 a quantitative evaluation of the quality of a TCO by the calculation of a figure of merit factor Q_H , according to the given equation:

$$Q_H = \frac{T^{10}}{R_s} \quad (18)$$

where T is the transmittance in the visible spectral region and R_s is the sheet resistance. However, this definition does not take into account the variations in thickness. Gordon [50] therefore introduced another figure of merit, FOM, defined by the equation:

$$\text{FOM} = \frac{\sigma}{\alpha} \quad (19)$$

where σ is the film conductivity and α the absorption in the visible region. Figure 9 shows the variation of the figure of merit, FOM, using Gordon formulation for the ITO samples with different deposition times before and after annealing. The conductivity was deduced from the resistivity values in table 2 and the absorption coefficient α used was the absorption around 2 eV.

As shown in figure 9, the obtained FOM of samples is in good agreement with literature [50,51]. It can be seen that the figure of merit decreases with the increase in the thickness before annealing. FOM has a maximum value for 15 min sample before annealing, but it decreases considerably after annealing due to the increase in resistivity (table 2). The 30-min sample has an acceptable figure of merit for TCO applications and is almost stable after annealing. This is due to its no sensitivity to the oxygen post-contamination that resulted from its (400) orientation. This confirms its performance as a long-term selective layer.

4. Conclusion

ITO thin films with different thicknesses were elaborated by PVD DC sputtering using Argon plasma without oxygen in the sputtering process and were subjected to thermal air annealing treatment for properties improvement. Specifically, deposition time and thermal annealing effect on structural, optical and electrical proprieties of the elaborated samples was investigated. Raman spectroscopy study analysis indicated a crystallinity of ITO films that varies with deposition time and annealing. SnO_2 vibration modes were identified from 575 cm^{-1} peak, which has disappeared after annealing for 30- and 60-min deposited thin films. This

result is a strong indicator of crystallinity improvement. The obtained XRD results also confirmed this behaviour. In fact, the elaborated ITO films have a cubic structure with (222) preferential direction. The film obtained after 30-min deposition time exhibited an additional intensive peak (400) corresponding to a higher surface roughness. Optical transmission measurement showed a high transparency, which is improved after annealing to rich 90%, and interference fringes were not observed in the spectra. The optical constants and the thicknesses were accurately determined from the transmission spectra using an efficient PSO algorithm-based method developed in this study. The film thicknesses obtained was from 3 to 173 nm with varying deposition time from 5 to 60 min. The refractive index decreased with increasing deposition time. After annealing, the ITO samples refractive index decreased and had almost the same static refractive index. The absorption coefficient decreased when increasing the deposition time. Optical study has proved also that the absorption after annealing decreased which indicates an improvement of transparency. The Hall effect measurements results as function of deposition time showed that the mobility increases before annealing and the films have very similar values of mobility after annealing. The electrical characterization showed also that before annealing, carrier density decreases and the resistivity increases with the thickness; however, an inverse behaviour was noticed for the charge carrier density variation after thermal treatment. Annealing has considerably decreased the resistivity of the layer obtained after 60-min deposition time. The 30-min layer exhibits less resistivity and figure of merit variations after air annealing due to the presence of the (400) orientation, which was around $4 \times 10^{-3} \Omega \text{ cm}$. Finally, the optical properties of ITO samples were related to the variation of the charged carrier density. A shift of the absorption edge towards shorter wavelengths was observed and was accompanied with an increase in the optical bandgap attributed to the charged carrier density increase. The value of effective mass deduced from the linear dependence between the optical gap and carrier concentration of $m^* = 0.86 m_0$ was obtained for the samples before annealing and $m^* = 0.76 m_0$ after air annealing.

References

- [1] Lewis B G and Paine D C 2000 *MRS Bull.* **25** 22
- [2] Alam M and Cameron D 2000 *Thin Solid Films* **377** 455
- [3] Chen B, Lin X, Cheng L, Lee C-S, Gambling W A and Lee S-T 2001 *J. Phys. D* **34** 30
- [4] Nomoto J-I, Konagai M, Okada K, Ito T, Miyata T and Minami T 2010 *Thin Solid Films* **518** 2937
- [5] Afre R A, Sharma N, Sharon M and Sharon M 2018 *Rev. Adv. Mater. Sci.* **51** 79
- [6] Sofi A, Shah M and Asokan K 2018 *J. Electron. Mater.* **47** 1344
- [7] Ohta H, Orita M, Hirano M, Tanji H, Kawazoe H and Hosono H 2000 *Appl. Phys. Lett.* **76** 2740
- [8] Yang C, Yang J, Han D, Li C, Xu Y and Qiu Y 2020 *E3S Web of Conferences*, 01039
- [9] Dong L, Zhu G, Xu H, Jiang X, Zhang X, Zhao Y *et al* 2019 *J. Mater. Sci. Mater. Electron.* **30** 8047
- [10] Mohammed Ali M K, Ibrahim K, Pakhuruddin M and Faraj M 2012 *Adv. Mater. Res.* **545** 393
- [11] Socol M, Preda N, Rasoga O, Costas A, Stanculescu A, Breazu C *et al* 2019 *Coatings* **9** 19
- [12] Wei L and Shuying C 2011 *J. Semicond.* **32** 013002
- [13] Parida B, Gil Y and Kim H 2019 *J. Nanosci. Nanotechnol.* **19** 1455
- [14] Pankratz J M 1972 *J. Electron. Mater.* **1** 181
- [15] Mizunashi M 1980 *Thin Solid Films* **70** 91
- [16] Minami T, Sonohara H, Kakumu T and Takata S 1995 *Thin Solid Films* **270** 37
- [17] Torkaman N, Ganjkanlou Y, Kazemzad M, Dabaghi H and Keyanpour-Rad M 2010 *Mater. Charact.* **61** 362
- [18] Chen A, Zhu K, Zhong H, Shao Q and Ge G 2014 *Sol. Energy Mater. Sol. Cells* **120** 157
- [19] Kennedy J and Eberhart R 1995 *Proceedings of ICNN'95-International Conference on Neural Networks* 1942
- [20] Lekoui F, Amrani R, Filali W, Garoudja E, Sebih L, Bakouk I E *et al* 2021 *Opt. Mater.* **118** 111236
- [21] Diéguez Barrientos À, Romano Rodríguez A, Vilà i Arbonès A M and Morante i Leonart J R 2001 *J. Appl. Phys.* **90** 1550
- [22] Lee H-C and Park O O 2006 *Vacuum* **80** 880
- [23] Prepelita P, Filipescu M, Stavarache I, Garoi F and Craciun D 2017 *Appl. Surf. Sci.* **424** 368
- [24] Seong S, Jung Y C, Lee T, Park I-S and Ahn J 2018 *Mater. Sci. Semicond. Process.* **79** 14
- [25] Le A H T, Dao V A, Pham D P, Kim S, Dutta S, Nguyen C P T *et al* 2019 *Sol. Energy Mater. Sol. Cells* **192** 36
- [26] Shakiba M, Kosarian A and Farshidi E 2017 *J. Mater. Sci. Mater. Electron.* **28** 787
- [27] Dong L, Chen Y, Zhu G, Xu H, Song J, Zhang X *et al* 2020 *Mater. Lett.* **260** 126735
- [28] Lekoui F, Hassani S, Ouchabane M, Akkari H, Dergham D, Filali W *et al* 2021 *Braz. J. Phys.* **51** 544
- [29] Rezaie M N, Manavizadeh N, Abadi E M N, Nadimi E and Boroumand F A 2017 *Appl. Surf. Sci.* **392** 549
- [30] Kim H, Gilmore A C, Pique A, Horwitz J, Mattoussi H, Murata H *et al* 1999 *J. Appl. Phys.* **86** 6451
- [31] Amrani R, Pichot F, Podlecki J, Foucaran A, Chahed L and Cuminal Y 2012 *J. Non-Cryst. Solids* **358** 1978
- [32] Poruba A, Fejfar A, Remeš Z, Špringer J, Vaněček M, Kočka J *et al* 2000 *J. Appl. Phys.* **88** 148
- [33] Li J, Jiang L, Chen M, Li X, Wei Y, Ma Y *et al* 2019 *Ceram. Int.* **45** 16214
- [34] Manificier J, Gasiot J and Fillard J 1976 *J. Phys. E: Sci. Instrum.* **9** 1002
- [35] Swanepoel R 1983 *J. Phys. E: Sci. Instrum.* **16** 1214
- [36] Garoudja E, Amrani R, Filali W, Lekoui F, Oussalah S, Cuminal Y *et al* 2021 *Optik* **241** 167030
- [37] Eberhart R and Kennedy J 1995 *MHS'95. Proceedings of the Sixth International Symposium on Micro Machine and Human Science* 39
- [38] Ruan Z-H, Yuan Y, Zhang X-X, Shuai Y and Tan H-P 2016 *Sol. Energy* **127** 147

- [39] Khare A and Rangnekar S 2013 *Appl. Soft Comput.* **13** 2997
- [40] Jain N, Nangia U and Jain J 2018 *J. Inst. Eng. (India): B* **99** 407
- [41] Tauc J and Abeles F 1972 *Optical properties of solids. Optical properties of amorphous solids* (Amsterdam: North-Holland Publishing Company)
- [42] Song S, Yang T, Liu J, Xin Y, Li Y and Han S 2011 *Appl. Surf. Sci.* **257** 7061
- [43] Al-Kuhaili M 2020 *J. Mater. Sci. Mater. Electron.* **31** 2729
- [44] Abboud P, Martinez F, Amrani R, Habib D, Parola S and Cuminal Y 2017 *J. Non-Cryst. Solids* **477** 42
- [45] Zhang K, Zhu F, Huan C and Wee A 1999 *J. Appl. Phys.* **86** 974
- [46] Haines W G and Bube R H 1978 *J. Appl. Phys.* **49** 304
- [47] Ray S, Banerjee R, Basu N, Batabyal A and Barua A K 1983 *J. Appl. Phys.* **54** 3497
- [48] Ohhata Y, Shinoki F and Yoshida S 1979 *Thin Solid Films* **59** 255
- [49] Haacke G 1976 *J. Appl. Phys.* **47** 4086
- [50] Gordon R G 2000 *MRS Bull.* **25** 52
- [51] Ali H M, Mohamed H A and Mohamed S H 2005 *Eur. Phys. J.-Appl. Phys.* **31** 87